Sujeet K. Sinha
N. Satyanarayana
Seh Chun Lim
Editors

Nano-tribology and Materials in MEMS

Springer

Nano-tribology and Materials in MEMS

Sujeet K. Sinha · N. Satyanarayana
Seh Chun Lim
Editors

Nano-tribology and Materials in MEMS

Springer

Editors
Sujeet K. Sinha
Department of Mechanical Engineering
Indian Institute of Technology
Kanpur
India

N. Satyanarayana
Seh Chun Lim
Department of Mechanical Engineering
National University of Singapore
Singapore

ISBN 978-3-642-36934-6 ISBN 978-3-642-36935-3 (eBook)
DOI 10.1007/978-3-642-36935-3
Springer Heidelberg New York Dordrecht London

Library of Congress Control Number: 2013934533

Printed on acid-free paper

Springer is part of Springer Science+Business Media (www.springer.com)

Preface

The field of nanotribology has advanced to a great extent thanks to the phenomenal growth of information storage industry. The magnetic hard disks used for recording and retrieving digital data require extremely thin nanolubricant for the protection of the disk from mechanical damages and wear by the slider which flies just above the surface of the disk with flying height only a few nanometer. Even though the slider is designed not to touch the disk, contacts between the slider and the disk are inevitable and hence we require the protection of the disk by the nanolubricant. A similar requirement, at least in length scale, is experienced in microsystems such as micro-electro-mechanical systems (MEMS) where micron-sized components, usually made of Si, are made to move about just like their macro-machine counterparts. Sliding, contact and impact between the components lead to the problems of adhesion, friction and wear. Because of the small length scales involved, the problems of tribology faced in microsystems differ drastically from those of the traditional macro-scale machines. Therefore, it is important to address these issues taking into considerations the materials, micro-fabrication process, lubricants and the lubrication methods.

A symposium titled "Nano-tribology and Related Materials Issues in MEMS" was organized by the Department of Mechanical Engineering, National University of Singapore from 13 to 14 May 2010. A number of invited talks were presented covering the fundamental nanotribology concepts, applications of new materials, surface modifications of Si and polymer substrates and simulations of the friction phenomenon under light load conditions. This book is a collection of the papers that were submitted by the presenters with some additional contributions by the experts in this field. Each chapter has been carefully selected and edited to bring out current practices in the MEMS tribology field with the explicit aim of finding appropriate solutions to the tribological problems faced in MEMS and nano-scale machines.

The editors would like to express their deepest appreciations to the invited and poster presenters of this symposium without whose help this event would not have been a reality. We thank the Dean, Faculty of Engineering and the Head of the Department of Mechanical Engineering, NUS, who provided all the supports needed for the organization of this event. We are also grateful to the Singapore

National Research Foundation (NRF) for the generous research grant (Award no.: NRF-CRP 2-2007-04) to our team which helped to support much of the research works that were presented in this symposium. Finally, we would like to thank the publisher and the authors of the chapters whose relentless effort through the manuscript preparation and editing has resulted in this compilation of very relevant works in the field of nanotribology and materials for MEMS. We earnestly hope that this edited book will positively add to the expanding literature in this field to help in current and future research.

April 2013

Sujeet K. Sinha
Nalam Satyanarayana
Seh Chun Lim

Contents

Chapter 1
Nanotribological Phenomena, Principles and Mechanisms for MEMS

Biswajit Saha, Erjia Liu and Shu Beng Tor

Abstract Nanotribology is referred to as a branch of tribology, which involves the interactions between two relatively moving materials in contact at a nanometer or an atomic scale. Nanotribology was stimulated by the fabrication of micro-electro-mechanical systems (MEMS). With the advent of scanning force microscopy (SPM), experimental approach to nanotribological regimes has been substantially advanced. Most common examples of nanotribological phenomena are in hard disk drives, MEMS, and nano-electro-mechanical systems (NEMS). Tribology is a surface phenomenon, which can be significantly affected by a very high surface-to-volume ratio in a micro or nanostructure. Small mass, light load, elastic deformation, and slight wear or absence of wear are typical of nanotribology. It has been widely perceived that various tribological test conditions, such as load, velocity, temperature, surface free energy, surface topography, environment, etc. play major roles in nanotribology. The experimental study of nanotribology is made possible by using surface force apparatus (SFA), atomic force microscope (AFM), friction force microscope (FFM), and ball-on-disk nanotribometer. Tribology research exceedingly needs broadened knowledge in various fields such as physics, chemistry, mechanics, materials science, etc. This chapter discusses the various aspects of nanotribology including nanofriction, nanowear and nanolubrication for MEMS. The nanotribological measurement methodologies and mathematical relationships between friction, bending and torsion forces based on AFM/LFM (lateral force microscopy) are comprehensively reviewed. The influences of various experimental conditions on nanotribology are described with various examples. Simulation techniques for nanotribology are also highlighted.

B. Saha · E. Liu (✉) · S. B. Tor
School of Mechanical and Aerospace Engineering,
Nanyang Technological University, 50 Nanyang Avenue,
Singapore 639798, Singapore
e-mail: mejliu@ntu.edu.sg

S. K. Sinha et al. (eds.), *Nano-tribology and Materials in MEMS*,
DOI: 10.1007/978-3-642-36935-3_1,

Contents

Introduction

The scientific term "tribology" is related to the interface of moving surfaces, which mainly deals with friction, wear and lubrication. Friction is resistance to relative motions of any state of materials in contact, wear is loss of materials from one solid body or another or both during their relative motions in contact, and lubrication is to reduce friction and wear between two moving materials by means of a lubricant present at the interface. Though tribological phenomena have existed since the very beginning of the world, the term "tribology" was only introduced by Jost in the modern age, i.e. 1966 [1]. This term has been more on technological use in industrial operation for economy, durability, lifetime and maintenance calculation.

Great progresses have been achieved in all the three fields of tribology during last few decades. Da Vinci, Amonton and Coulomb [1] have found that friction is proportional to applied load but independent of contact area and velocity, which is more applicable for hard solid materials. However, many researchers have found that friction of soft materials, such as polymeric materials, is significantly affected by real area of contact, surface adhesion and temperature. Hammerschmidt et al. [2] have reported that polymeric materials can show a special kind of friction behavior because of the structural relaxation of their molecular chains governed by energy dissipation and correlated frictional response with glass-to-rubber transition and secondary relaxation mechanisms. Enachescu et al. [3] have found that the tribological behavior of materials is a function of applied load, based on an observation that friction is directly proportional to the real area of contact. Exceptions of Amonton's law ($F = \mu.W$) have also been encountered by many other researchers [4–6].

Nanotribology is referred to as a branch of tribology, which involves the interactions between two relatively moving materials in contact at a nanometer or atomic scale, where atomic forces are one of the most dominating forces. Tribology is a surface phenomenon, which can be significantly affected by a very high surface-to-volume ratio in a micro or nanostructure.

The demand of society's particular needs in advanced technologies has been gradually increasing. The advent of micro and nanotechnologies has greatly motivated researchers' interest in designing novel and complex architectures. A proper understanding of nanotribological behavior is very important to improve the applicability and lifetime of tiny architectures and to protect micro and nanosystems from severe friction and wear.

Most common examples of nanotribological phenomena are in magnetic recording disk drives, micro-electro-mechanical systems (MEMS), and nano-electro-mechanical systems (NEMS). Small mass, light load, elastic deformation, and slight wear or absence of wear are typical of nanotribology. The experimental study of nanotribology is made possible by surface force apparatus (SFA), atomic force microscope (AFM), friction force microscope (FFM), and ball-on-disk nanotribometer.

Tribological properties of materials depend on the true area of contact between the contacting surfaces. Thus, roughness is one of the important affecting parameters and is also found to be a function of various parameters such as surface energy, velocity, humidity, environment, and temperature [2, 7–11].

This chapter deals with the various aspects of nanotribology including nanofriction, nanowear and nanolubrication for MEMS. The nanotribological measurement methodologies and mathematical relationships between friction, bending and torsion forces based on AFM/LFM (lateral force microscopy) are comprehensively presented. The influences of various parameters on nanotribology are described with various examples. Simulation techniques for nanotribology are also overviewed.

Measurement Techniques

Limitation of scanning tunneling microscopy (STM) leads to the invention of AFM by Binning et al. [12] in 1986. The basic working principle of AFM is schematically shown in Fig. 1.1, in which a laser light is reflected from the rear side of a cantilever to the position sensitive photodiode detector to record the movement of the cantilever. Any deflection or torsion of the cantilever causes a change in the laser path so does in the photodiode detector as shown in Fig. 1.2.

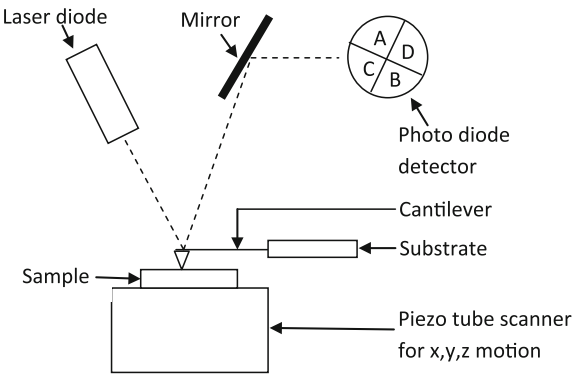

Fig. 1.1 Schematic operating principle of a typical AFM. The scanning position of a sample is controlled by a piezo controller. A laser light is reflected from the rear side of the cantilever to a photodiode detector to detect the bending and torsion of the cantilever

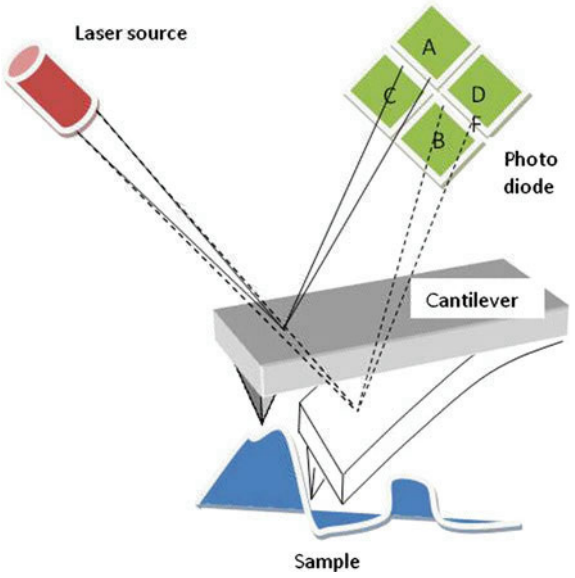

Fig. 1.2 A schematic AFM tip scanning over a sample. The acting force on the tip is determined by using a quadrant photodiode detector to measure the deflection and torsion of the cantilever

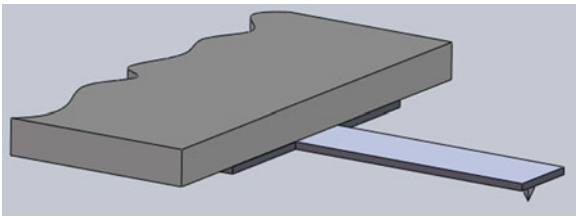

Fig. 1.3 Schematic diagram of rectangular cantilever

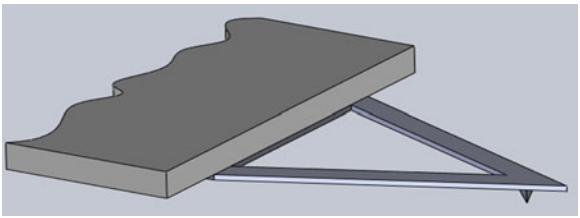

Fig. 1.4 Schematic diagram of V-shape cantilever

Importance of AFM Cantilever

Most AFM cantilevers are made of Si, Si_3N_4 or SiO_2, which work based on the knowledge of their spring constants (k_s). The k_s and resonance frequency (f_0) of a cantilever beam with a rectangular cross-section loaded at its flexible end can be determined by the following equations:

$$k_s = \frac{Ebt^3}{4l^3} \tag{1.1}$$

$$f_0 = 0.162\sqrt{\frac{E}{\rho}} \times \frac{t}{l^2} \tag{1.2}$$

where E, b, t, l and ρ are Young's modulus, width, thickness, length and density of the cantilever, respectively.

A simple method of static deflection of a cantilever under the force of a known mass is usually used to determine its spring constant and commercially available cantilevers are generally supplied with this information. Rectangle and triangle (V) shaped cantilever beams are two basic cantilever geometries as shown in Figs. 1.3 and 1.4, both of which are suitable for contact, intermittent contact and non-contact modes of operation. A higher mechanical stability with respect to lateral distortion makes V-shape cantilevers more preferable for contact mode AFM. In the contact mode AFM, repulsive and attractive forces acting on the cantilever depend upon the distance between AFM tip and sample surface. In the attractive regime, dominating forces are van der Waals, electrostatic, magnetic and capillary forces, which give the information about surface topography, distribution of

charges, magnetic domain wall structure, or liquid film distribution. At a separation distance of a few angstroms, active repulsive forces allow the sample surface topography to be traced with atomic resolutions, where the cantilever acts as a force transducer. However, in the case of lateral force microscopy (LFM), where tortional signals are the main domain of interest, rectangular cantilevers are thus more preferable because of their higher sensitivities to lateral forces.

A proper selection of cantilever is important, which depends on a particular application for which the cantilever will be used. In the contact mode, a large applied force on cantilever can inelastically deform or modify the sample surface. However, for a hard sample, modification of the cantilever tip is more likely than that of the sample surface. This problem can be solved by using a cantilever of lower spring constant. However in noncontact and intermittent contact modes, a cantilever with higher stiffness and resonance frequency is preferable, which can prevent from contacting with and sticking to the sample surface and result in a higher signal-to-noise ratio.

The critical design criteria of contact mode AFM cantilevers include small mass (e.g. <0.1 μg), short lever length (e.g. <200 μm), small beam thickness (e.g. <0.5 μm), low bending stiffness for higher flexibility and sensitivity, high thermal stability, mechanical stability (e.g. resonant frequency >2 kHz) and torsion elastic constant, a sharp protruding tip, and a mirror or electrode for reflecting deflection and torsion signals.

The thermal distortion of a cantilever beam is

$$\frac{d\varepsilon}{dx} = \frac{\alpha dT}{dx} = \left(\frac{\alpha}{\lambda}\right) q \tag{1.3}$$

where ε, α, T, λ and q $\left(= \lambda \frac{dT}{dx}\right)$ are the thermal strain, thermal expansion coefficient, temperature, thermal conductivity, and heat input, respectively.

$\frac{d\varepsilon}{dx}$ of a beam is proportional to α and inversely proportional to λ of the beam. Therefore, $\frac{d\varepsilon}{dx}$ of a beam can be minimized by maximizing $\left(\frac{\lambda}{\alpha}\right)$.

The mass of a rectangular cantilever beam having a uniform cross-section can be represented by

$$m = Al\rho \ \text{(Kg)} \tag{1.4}$$

where m, A, and ρ are the mass, cross-section area and density, respectively.

Relations among the deflection, bending force and spring constant of a cantilever beam are

$$\delta = F_{bend} l^3 / C_1 EI \ \text{(m)} \tag{1.5}$$

$$k = F_{bend} / \delta \ \text{(N/m)} \tag{1.6}$$

$$\text{with } I \propto A^2 \ \text{(m}^4\text{)} \tag{1.7}$$

Here δ, F_{bend}, C_1, I, and k are the beam deflection, bending force, constant, second moment of area, and spring constant, respectively.

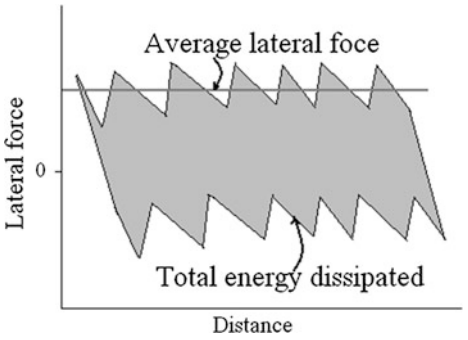

Fig. 1.5 Schematic diagram of lateral force versus scan distance by LFM

Thus, the mass of the beam can be expressed as

$$m = \left(\frac{12k}{C_1 l}\right)^{1/2} l^3 \left(\frac{\rho}{E^{1/2}}\right) \text{(Kg)} \tag{1.8}$$

which can be minimized by maximizing

$$\left(E^{1/2}/\rho\right) \tag{1.9}$$

Lateral Force Microscope

One of the capabilities of contact mode AFM is to study the lateral forces or tribological properties between sample and AFM tip in contact and relative motion [13]. In this regard, AFM is known as lateral force microscope (LFM) or FFM. LFM has some advantages over conventional tribometer. LFM has an ability to quantify nanotribological properties at nano or atomic scale, such as interaction forces, i.e. attractive and repulsive forces. A big advantage of LFM is that most materials can be investigated under their natural conditions, including biological samples in an aqueous environment. In the schematic diagram shown in Fig. 1.5, a lateral force loop is used to determine the frictional behavior of a material surface in contact with a LFM tip, and the area inside the loop indicates a total dissipated energy. The measured lateral forces depend on the applied normal forces and the local and average friction coefficients can be calculated by dividing the respective local and average lateral forces by the applied normal forces. The specialty of LFM is that as the distance scale can be very small it is able to identify the friction properties of materials with atomic resolutions, which allows LFM to map the composition distribution of a material surface.

The four-sector photodiode detector of LFM as shown in Fig. 1.1 can simultaneously detect both deflection and torsion signals of the cantilever. A schematic measuring principle of vertical and lateral movements of the tip is shown in Fig. 1.6, where the vertical motion of the tip is detected by the photodiode pair A and B while the lateral motion of the tip is monitored by the pair C and D [14].

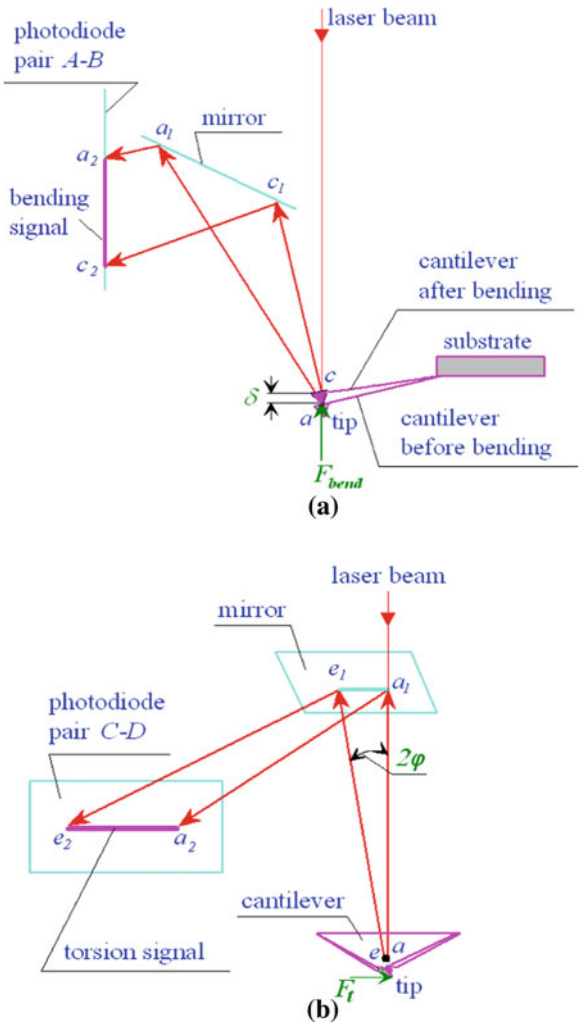

Fig. 1.6 Schematic diagrams of **a** bending and **b** torsion signals of cantilever. (Reprinted with permissions from Liu et al. [14] and Liu [15])

A voltage signal measured by the photodiodes C and D, which is a result of torsion, is converted to a lateral tangential displacement of the cantilever tip as schematically shown in Fig. 1.6b. The resulted lateral tangential force is then calculated from the product of the torsion elastic constant of the cantilever and the lateral tangential displacement of the tip.

Bending of Rectangular Cantilever

Figure 1.7a and b show the front and side views of a rectangular cantilever. The deflection of the cantilever beam caused by the bending force F_{bend} is

shown in Fig. 1.8a, where the curvature of the beam along the x-direction can be derived as

$$\frac{d^2z}{dx^2} = \frac{M_y}{EI_y} \tag{1.10}$$

with

$$M_y = F_{bend}x \text{ (Nm)}, \ (0 \le x \le l) \tag{1.11}$$

and

$$I_y = \frac{bt^3}{12} \text{ (m}^4\text{)} \tag{1.12}$$

where M_y is bending moment of the cantilever beam about the y-axis, I_y is the second moment of area of the beam, E is Young's modulus of the beam material, and l, b and t are the length, width and thickness of the beam.

Integration of Eq. 1.10 is represented by Eq. 1.13,

$$\begin{aligned} z' &= \int \frac{M_y}{EI_y}dx = \int \frac{F_{bend}x}{EI_y}dx \\ &= \frac{F_{bend}}{EI_y}\left(\frac{x^2}{2} + C_1\right) \end{aligned} \tag{1.13}$$

with the slop of the beam at $x = l$ being zero.

Therefore, $z'|_{x=l} = \frac{F_{bend}}{EI_y}\left(\frac{l^2}{2} + C_1\right) = 0$, from which

$$C_1 = -\frac{l^2}{2}. \tag{1.14}$$

Thus,

$$z' = \frac{F_{bend}}{2EI_y}\left(x^2 - l^2\right) \tag{1.15}$$

Integration of Eq. 1.15 is presented as Eq. 1.16,

$$\begin{aligned} z &= \int z'dx = \int \frac{F_{bend}}{2EI_y}\left(x^2 - l^2\right)dx \\ &= \frac{F_{bend}}{2EI_y}\left(\frac{x^3}{3} - l^2x + C_2\right) \text{ (m)} \end{aligned} \tag{1.16}$$

Because of the zero deflection of the beam at $x = l$, $z|_{x=l} = \frac{F_{bend}}{2EI_y}\left(\frac{l^3}{3} - l^3 + C_2\right) = \frac{F_{bend}}{2EI_y}\left(-\frac{2l^3}{3} + C_2\right) = 0$,

$$C_2 = \frac{2l^3}{3} \tag{1.17}$$

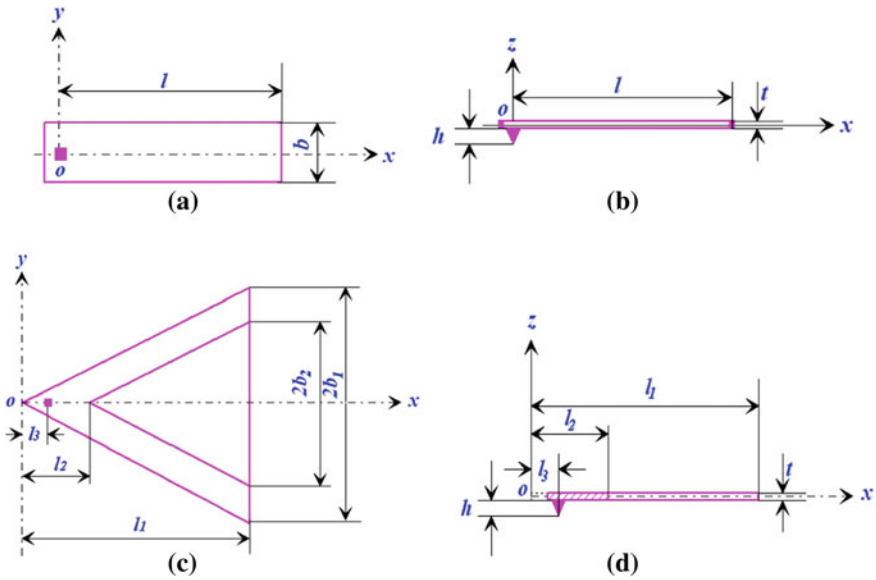

Fig. 1.7 Schematic diagrams of **a** front and **b** side views of rectangular cantilever and **c** front and **d** side views of V-shaped cantilever. (Reprinted with permissions from Liu et al. [14] and Liu [15])

Therefore, Eq. 1.16 is rewritten as,

$$z = \frac{F_{bend}}{2EI_y}\left(\frac{x^3}{3} - l^2x + \frac{2l^3}{3}\right) \text{ (m)} \tag{1.18}$$

The deflection of the cantilever beam (δ) at the tip position (x = 0) is

$$\delta = z|_{x=0} = \frac{F_{bend}}{2EI_y}\left(\frac{2l^3}{3}\right) = \frac{F_{bend}l^3}{3EI_y} \text{ (m)} \tag{1.19}$$

Thus, the bending elastic constant of the rectangular cantilever is

$$k = \frac{F_{bend}}{\delta} = \frac{3EI_y}{l^3} = \frac{3Ebt^3}{12l^3} = \frac{Ebt^3}{4l^3}\left(\frac{\text{N}}{\text{m}}\right) \tag{1.20}$$

Bending of V-Shaped Cantilever

The schematic diagrams of the front and side views of a V-shaped cantilever are shown in Fig. 1.7c and d and the corresponding deflected and distorted ones are shown in Fig. 1.8c and d.

The curvature of the cantilever at any point along the x-axis is

$$\frac{d^2z}{dx^2} = \frac{M_y}{EI_y} \tag{1.21}$$

with

$$M_y = F_{bend}(x - l_3)\ (\text{Nm}),\ (0 \le x \le l_1) \tag{1.22}$$

$$I_{y1} = \frac{(b_1 - b_2)t^3}{6}\ (\text{m}^4),\ (l_2 \le x \le l_1) \tag{1.23}$$

and

$$I_{y2} = \frac{b_1 t^3 x}{6l_1}\ (\text{m}^4),\ (l_3 \le x \le l_2) \tag{1.24}$$

where b_1 and b_2 are the beam widths of different segments and l_1, l_2 and l_3 are the beam lengths of different segments.

After integrating Eq. 1.21,

$$\begin{aligned} z &= z_1 + z_2 \\ &= \iint\limits_{(l_2 \le x \le l_1)} \frac{M_y}{EI_{y1}}dx^2 + \iint\limits_{(l_3 \le x \le l_2)} \frac{M_y}{EI_{y2}}dx^2 \\ &= \frac{6F_{bend}}{E(b_1 - b_2)t^3} \iint\limits_{(l_2 \le x \le l_1)} (x - l_3)dx^2 + \frac{6F_{bend}l_1}{Eb_1t^3} \iint\limits_{(l_3 \le x \le l_2)} \frac{(x - l_3)}{x}dx^2 \end{aligned} \tag{1.25}$$

The boundary conditions for Eq. 1.25 are: $z_1 = z_1{}' = 0$ at $x = l_1$, $z_1 = z_2$ at $x = l_2$, and $z_1{}' = z_2{}'$ at $x = l_2$. Therefore the deflection of the V-shaped cantilever at the tip position ($x = l_3$) is

$$\begin{aligned} \delta &= z|_{x=l_3} \\ &= \frac{F_{bend}}{Et^3}\left\{\frac{3l_1\left[l_2^2 - 4l_2l_3 + 2l_3^2\ln(l_2/l_3) + 3l_3^2\right]}{b_1} + \frac{2\left[l_1^3 - l_2^3 - 3l_3\left(l_1^2 - l_2^2\right) + 3l_3^2(l_1 - l_2)\right]}{b_1 - b_2}\right\} \end{aligned} \tag{1.26}$$

Thus, the normal bending elastic constant of V-shaped cantilever can be expressed as

$$\begin{aligned} k &= \frac{F_{bend}}{\delta} \\ &= Et^3\left(\left\{\frac{3l_1\left[l_2^2 - 4l_3l_2 + 2l_3^2ln(l_2/l_3) + 3l_3^2\right]}{b_1} + \frac{2\left[l_1^3 - l_2^3 - 3l_3\left(l_1^2 - l_2^2\right) + 3l_3^2(l_1 - l_2)\right]}{b_1 - b_2}\right\}\right)^{-1} \end{aligned} \tag{1.27}$$

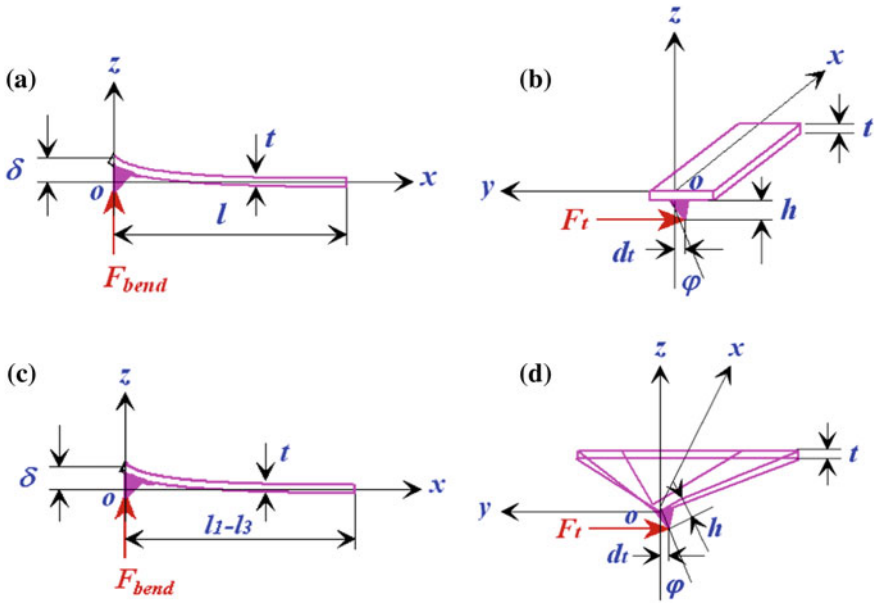

Fig. 1.8 Schematic diagrams of **a** rectangle cantilever deflected by normal bending force F_{bend} and **b** distorted by lateral force F_t, and **c** V-shaped cantilever deflected by F_{bend} and **d** distorted by F_t. (Reprinted with permissions from Liu et al. [14] and Liu [15])

Torsion of Rectangular Cantilever

When the rectangular beam is distorted by a lateral force F_t (Fig. 1.8b), the first derivative of torsion angle is expressed as

$$\frac{d\varphi}{dx} = \frac{T}{GJ}, (0 \le x \le l) \tag{1.28}$$

with

$$T = F_t(h + t/2)\ (\text{Nm}) \tag{1.29}$$

and

$$J = b^3t^3/3.6\left(b^2 + t^2\right)\ (\text{m}^4) \tag{1.30}$$

where: φ, T, h, G, and J are torsion angle, torsion moment, tip height, shear modulus, and polar moment of inertia, respectively.

By integrating Eq. 1.28, the torsion angle of the cantilever beam at the tip position ($x = 0$) is shown as

$$\varphi = \int_{l}^{0} \frac{T}{GJ} d(l-x) = \int_{0}^{l} \frac{F_t(h+t/2) \times 3.6(b^2+t^2)}{Gb^3t^3} dx$$
$$= \frac{3.6F_t l(h+t/2)(b^2+t^2)}{Gb^3t^3} \text{ (rad)} \tag{1.31}$$

The lateral tangential displacement of the tip is thus derived as

$$d_t = \left(h+\frac{t}{2}\right)\sin\varphi \approx \left(h+\frac{t}{2}\right)\varphi$$
$$= \frac{3.6F_t l(h+t/2)^2(b^2+t^2)}{Gb^3t^3} \text{ (m)} \tag{1.32}$$

and, the torsion elastic constant of the rectangular cantilever is

$$k_t = \frac{F_t}{d_t} = \frac{Gb^3t^3}{3.6l(h+t/2)^2(b^2+t^2)} \left(\frac{\text{N}}{\text{m}}\right) \tag{1.33}$$

Torsion of V-Shaped Cantilever

The distortion of the V-shaped cantilever caused by the lateral force F_t as shown is Fig. 1.8d can be represented, in a similar way to that of the rectangular cantilever, by Eq. 1.34.

$$\frac{d\varphi}{dx} = \frac{T}{GJ} \tag{1.34}$$

where the expression of torsion (T) is similar to Eq. 1.29. The polar moment of inertia of the beam can be represented as

$$J_1 = \frac{2t^3(b_1-b_2)}{3} \text{ (m}^4\text{)}, \ (l_2 \le x \le l_1) \tag{1.35}$$

and

$$J_2 = \frac{2t^3b_1x}{3l_1} \text{ (m}^4\text{)}, \ (l_3 \le x \le l_2) \tag{1.36}$$

where φ, T, G and J have their usual meanings.

The torsion angle of the cantilever beam at the tip position ($x = l_3$) is determined by integrating Eq. 1.34, which is presented as

$$\begin{aligned}\varphi &= \int_{l_2}^{l_1} \frac{T}{GJ_1}dx + \int_{l_3}^{l_2} \frac{T}{GJ_2}dx \\ &= \int_{l_2}^{l_1} \frac{3T}{2Gt^3(b_1 - b_2)}dx + \int_{l_3}^{l_2} \frac{3Tl_1}{2Gt^3 b_1 x}dx \\ &= \frac{3T}{2Gt^3(b_1 - b_2)}\int_{l_2}^{l_1} dx + \frac{3Tl_1}{2Gt^3 b_1}\int_{l_3}^{l_2} \frac{1}{x}dx \\ &= \frac{3F_t(h + t/2)}{2Gt^3}\left[\frac{1}{(b_1 - b_2)}\int_{l_2}^{l_1} dx + \frac{l_1}{b_1}\int_{l_3}^{l_2} \frac{1}{x}dx\right] \\ &= \frac{3F_t(h + t/2)}{2Gt^3}\left[\frac{l_1 - l_2}{b_1 - b_2} + \frac{l_1}{b_1}\ln\left(\frac{l_2}{l_3}\right)\right] \text{ (rad)}\end{aligned} \tag{1.37}$$

The tip lateral tangential displacement of the V-shaped cantilever for a very small φ is expressed as

$$\begin{aligned}d_t &= \left(h + \frac{\mathrm{t}}{2}\right)\sin\varphi \approx \left(h + \frac{\mathrm{t}}{2}\right)\varphi \\ &= \frac{3F_t(h + t/2)^2}{2Gt^3}\left[\frac{l_1 - l_2}{b_1 - b_2} + \frac{l_1}{b_1}\ln\left(\frac{l_2}{l_3}\right)\right] \text{ (m)}\end{aligned} \tag{1.38}$$

Therefore, the torsion elastic constant of the V-shaped cantilever is

$$k_t = \frac{F_t}{d_t} = \frac{2Gt^3}{3(h + t/2)^2\left[\frac{l_1 - l_2}{b_1 - b_2} + \frac{l_1}{b_1}\ln\left(\frac{l_2}{l_3}\right)\right]}\left(\frac{\mathrm{N}}{\mathrm{m}}\right) \tag{1.39}$$

Chemical Mapping and Topography Using Nanofriction

LFM is also a powerful tool to map the chemical composition and inhomogeneity of a sample surface. For a smooth surface, the variations in lateral distortion of the cantilever arise from the changes in friction sources. As schematically shown in

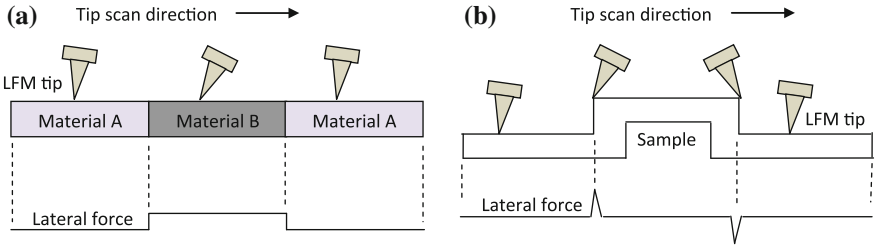

Fig. 1.9 Schematic diagrams of variations of lateral force due to variations in **a** composition and **b** topography of sample surfaces

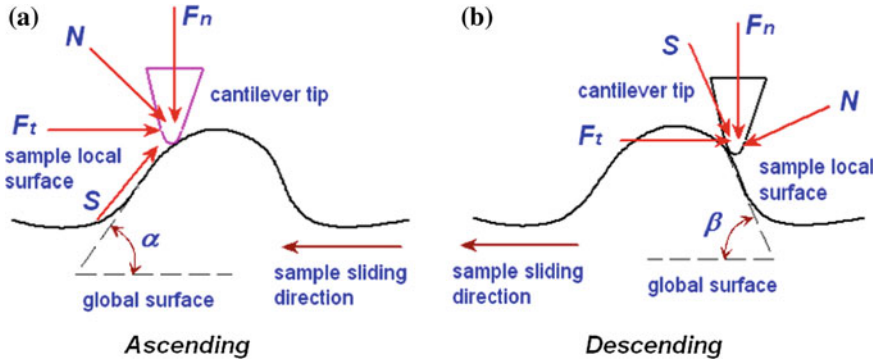

Fig. 1.10 Schematic diagrams of scanning LFM tip at a local asperity during **a** upward and **b** downward movements. (Reprinted with permissions from Liu [15] and Bhushan [16])

Fig. 1.9a a compound comprises different materials A and B. In the compound, if material B has a higher friction than material A against the tip, the friction by material B will cause a higher deflection of the cantilever when the tip scans through material B. The variations of the cantilever deflection are recoded as a LFM image corresponding to the different compositions in the compound and thus create a chemical map.

For a homogeneous material with a rough surface, lateral forces sensed by the cantilever vary according to the locations on the material surface as shown in Fig. 1.9b. Sudden changes in lateral force occur when the tip scans a local surface feature depending on whether it is an upward or downward traveling. Therefore for chemical mapping, a comparison with a topographical plot is very important.

The variations of local friction due to variations in surface topography can be calculated by incorporating the plowing effect in the calculation. An assumption is made for the tip radius smaller than the size of asperities. An upward movement of the tip causes an additional torsion in the cantilever beam, which induces a higher friction. However, a downward motion causes almost no additional torsion in the beam, which lowers the friction.

The local coefficient of friction during the upward movement of the tip under a normal load F_n at an asperity on the sample surface having a slope of α with respect to the global surface can be calculated using Eq. 1.40 based on the schematic shown in Fig. 1.10a.

$$\begin{aligned}\mu_1 &= \frac{F_t}{F_n} = \frac{S\cos\alpha + N\sin\alpha}{N\cos\alpha - S\sin\alpha} \\ &= \frac{\mu_0 + \tan\alpha}{1 - \mu_0\tan\alpha} \approx \mu_0 + \tan\alpha\end{aligned} \tag{1.40}$$

for a very small angle α, $\mu_0 \tan\alpha \ll 1$.

Here, S, N, F_t, and F_n are the shear force perpendicular to the local surface, normal force perpendicular to the local surface, friction force along the global

surface, and normal force perpendicular to the global surface, respectively. It is noted that the uphill plowing component (tan α) has a positive contribution to the local friction.

Similarly, the local coefficient of friction during the downward sliding at the same asperity having a slope of β with respect to the global surface can be determined based on the schematic shown in Fig. 1.10b:

$$\begin{aligned}\mu_2 &= \frac{F_t}{F_n} = \frac{S\cos\beta - N\sin\beta}{N\cos\beta + S\sin\beta} \\ &= \frac{\mu_0 - \tan\beta}{1 + \mu_0\tan\beta} \approx \mu_0 - \tan\beta\end{aligned} \tag{1.41}$$

for a very small angle β, $\mu_0 \tan\beta \ll 1$.

It is noted that the downhill plowing component (*tan* β) has a negative sign in Eq. 1.41.

For a symmetric asperity with $\beta = \alpha$, the average local coefficient of friction across the asperity is

$$\begin{aligned}\mu_{ave} &= \frac{\mu_1 + \mu_2}{2} \\ &= \frac{\mu_0(1 + \tan^2\alpha)}{1 - \mu_0^2\tan^2\alpha} \\ &\approx \mu_0\left(1 + \tan^2\alpha\right)\end{aligned} \tag{1.42}$$

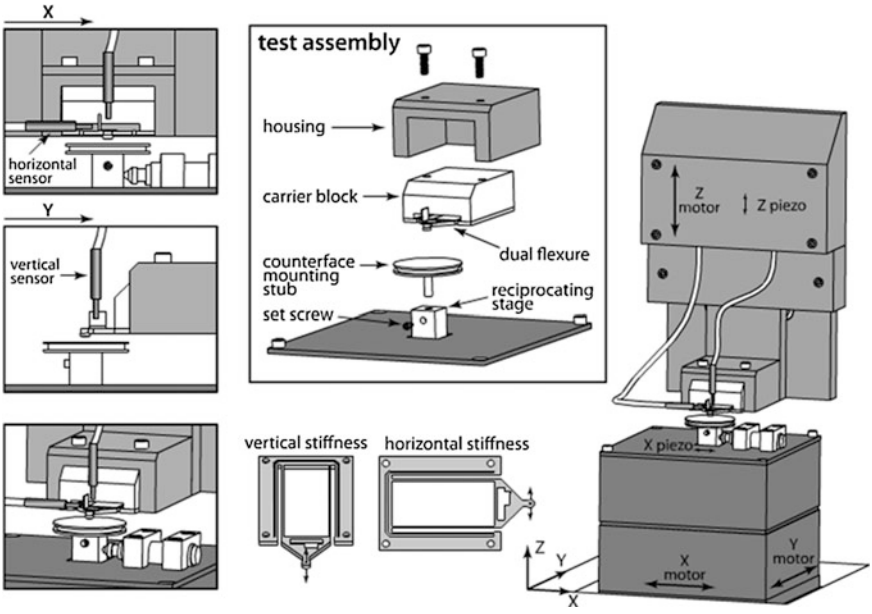

Fig. 1.11 A schematic diagram showing a nanotribometer along with its various components

for a very small angle α, $\mu_0^2 \tan^2 \alpha \ll 1$.

The plowing component of the local coefficient of friction is $\pm \tan \alpha$ in either moving direction depending on the scanning direction of the tip relative to the sample surface.

Nanotribometer

Nanotribometer is also used to measure friction coefficient of materials at nanoscales. A schematic diagram of a typical nanotribometer (CSM) together with its various components is shown in Fig. 1.11. Such a tribometer has certain advantages over LFM, such as high speed, wide load range and large traveling distance with both rotating and reciprocating operation modes. In such a system a specimen is mounted at the bottom and a flexible cantilever is mounted at the top. A z-piezo is used to control the movement of the cantilever up and down. Generally, two

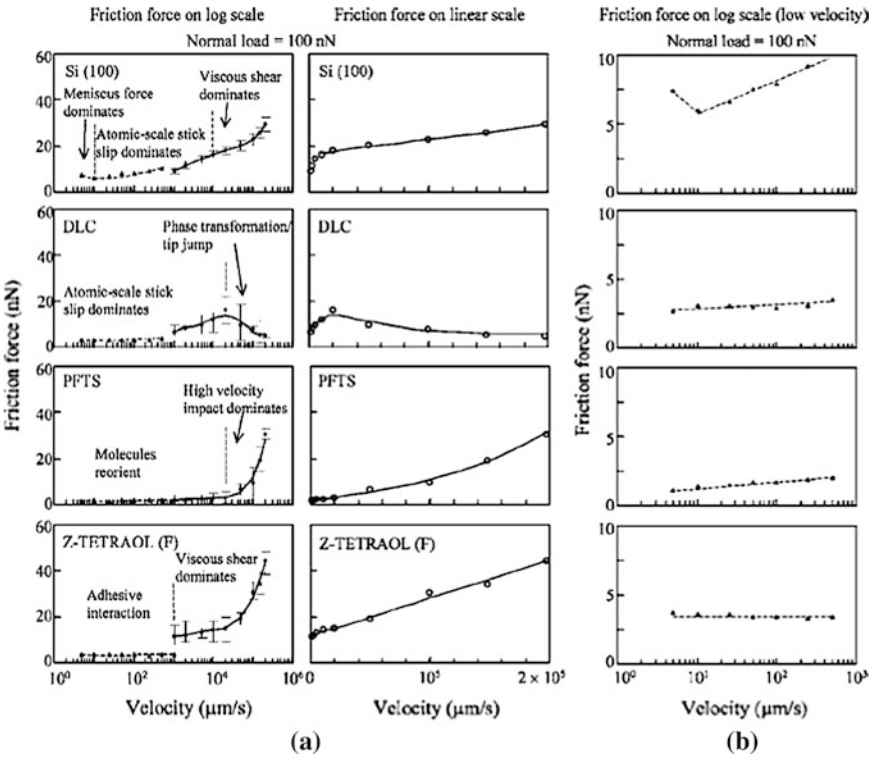

Fig. 1.12 Frictional force versus velocity at **a** both log and linear scales and **b** log scale in a range of lower velocities. (Reprinted with permission from Tao and Bhushan [17], Copyright 2007, American Vacuum Society) [17]

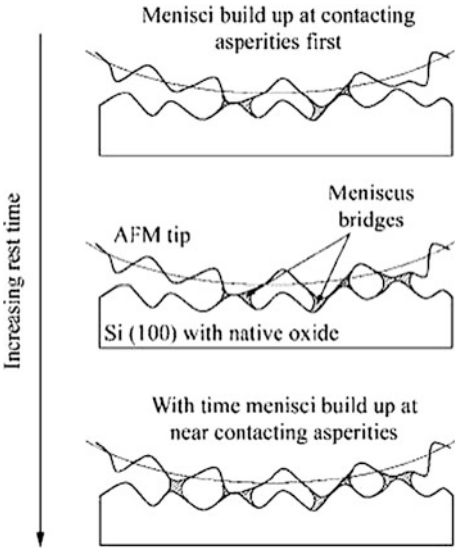

Fig. 1.13 Schematic diagram showing the effect of resting time on adhesive force due to formation of meniscus bridges in contact zone. (Reprinted with permission from Tambe and Bhushan [18])

force sensors are connected to the cantilever holder to measure the deflections of the cantilever in the x and z-directions. Two mirrors are attached to the flexible end of the cantilever, from which the force sensors detect the optical signals reflected from the mirrors. The measured reflected light intensity depends on the distances between the sensors and mirrors, which are proportional to the deflections of the cantilever caused by friction or adhesion. The lateral and vertical deflections of the cantilever are induced by the frictional and adhesion forces, respectively. Therefore, the corresponding spring constants of the cantilever are used to calculate friction or adhesion forces.

Controlling Parameters for Friction Coefficient

Effect of Velocity

A great influence of relative moving velocity of two bodies in contact on friction force or friction coefficient is shown in Fig. 1.12. Many researchers have studied friction force as a function of velocity for Si, diamond-like carbon (DLC) and many other materials [17, 18]. In the ambient condition a thin film of moisture can be formed on material surfaces, which affects friction coefficient in a range of low velocities. For example, the friction force between Si surface and AFM tip decreases with increasing velocity in a range of very low velocities, which is because the meniscus bridges developed around the tip are a function of equilibrium time as shown in Fig. 1.13. During the movement of the tip, it breaks the meniscus bridges, which generates a friction force. The generated friction force

depends on the strengths of the meniscus bridges. However, the meniscus bridges cannot be fully reformed when velocity is increased, which results in a lower meniscus force and thus a lower friction force as shown in Fig. 1.13.

At very high velocities, the meniscus bridges do not have enough time to form and thus their effect becomes negligible and the stick–slip becomes more dominating for controlling the friction coefficient. The stick–slip causes a linear increase in friction force with velocity, which can be explained by viscous shear.

The motion of the AFM tip is expressed by a spring mass model (Eq. 1.43) to explain the atomic scale stick–slip mechanism of friction [19]:

$$m\ddot{x}_t = -\eta\dot{x}_t - k(x_M - x_t) - F \tag{1.43}$$

with

$$x_m = v_m t \tag{1.44}$$

where m, η, k, x_t, F, x_m, v_m, and t are the effective mass of the system, viscous damping coefficient, spring constant of the cantilever, position of the tip, external force, equilibrium position of the cantilever, scan velocity, and rest time, respectively.

The lateral force is expressed as

$$F_l = k(x_M - x_t) \tag{1.45}$$

which is the friction force.

Tomlinson has assumed a periodic surface with a potential $V(x)$ as presented in Eq. 1.46 [20].

$$V(x) = V_0\left(1 - cos\frac{2\pi x}{a}\right) \tag{1.46}$$

where V_0 and a are the surface barrier potential height and lattice constant of the surface, respectively.

Therefore, the force F is expressed as

$$F = V'(x) = \frac{2\pi V_0}{a}\sin\left(\frac{2\pi x}{a}\right) \tag{1.47}$$

The Tomlinson model has taken into account the effect of thermal activation or elastic energy stored in the cantilever to derive the relationship between friction force and velocity, which is presented by Eq. 1.48:

$$F_{stick-slip} = F_0 + c\,ln\,v \tag{1.48}$$

where F_o and c are the constants and υ is the sliding velocity.

If a thin film of any liquid like water or moisture is present, the friction force is related to the velocity of the tip and the viscosity of the film as presented below:

$$F_{friction} = \mu N + \eta \dot{\gamma} A \approx \mu N + \frac{\eta v A}{d} \tag{1.49}$$

where μ, N, η, $\dot{\gamma}$, v, A, and d are the coefficient of friction at dry condition, applied load, viscosity of the film, velocity gradient, sliding velocity, real contact area, and thickness of the film, respectively.

Here, a noticeable thing is that a thin film of moisture on a material surface has been considered. This moisture layer depends on the surface nature of the material concerned such as hydrophilicity or hydrophobicity, which will be discussed later. Because of the formation and breaking of the menisci at lower velocities and the stick–slip mechanism at higher velocities, the friction force first decreases and then increases with the increase in velocity as shown in Fig. 1.12.

A moisture layer can be easily formed and the meniscus contribution is significant on a hydrophilic surface such as Si. In the contrast, the effect of meniscus bridges is not significant on some hydrophobic surfaces where the stick–slip is the dominating factor, which causes a continuous increase in coefficient of friction with the increase in velocity for these surfaces.

Effect of Surface Force

The nature of material surfaces plays a key role in controlling friction. An AFM tip can experience various kinds of forces, such as van der Waals, capillary, chemical bonding, magnetic, hydration and electrostatic forces, when it comes close to the counterbody. A basic equation of friction coefficient is the ratio of lateral force to normal force. Acting forces that increase or decrease the normal force according to the direction of action affect the friction force and friction coefficient. When the tip comes near the sample surface it feels an attractive force and when it almost touches the sample surface it feels a repulsive force, both of which contribute to the friction force accordingly.

Van der Waals forces are short-range attractive forces acting between all atoms, molecules, nanoparticles, etc. An AFM tip usually experiences van der Waals forces (F_{vdw}) when it is brought into close proximity to the sample surface, which is a function of distance (r_d) and tip radius (R_{tip}) as represented by Eq. 1.50:

$$F_{vdw} = A_{ham} R_{tip} / (6 r_d^2) \tag{1.50}$$

where A_{ham} is the Hamaker constant that depends on the polarizability of the material.

The acting electrostatic force (F_{el}) can be attractive or repulsive depending upon the charges, which is expressed as

$$F_{el} = (q_1 q_2) / (4\pi\varepsilon D_d^2) \tag{1.51}$$